RSC Advances

PAPER

View Article Online
View Journal | View Issue

Cite this: *RSC Adv.*, 2025, **15**, 34833

Efficient removal of selected neonicotinoids from single and combined systems using CuO/rGO modified *musa parasidiaca* biochar: insight into cost analysis

Ajibola A. Bayode, *[a] Stephen Sunday Emmanuel, [b] Hamza Badamasi, [c] Saheed O. Sanni, [d] Odunayo T. Ore, [e] Adewumi Oluwasogo Dada, [f] Obianuju Patience Ilo [g] and Ademidun Adeola Adesibikan[h]

The widespread use of neonicotinoid pesticides, particularly imidacloprid (IMI) and acetamiprid (ACE), has raised environmental concerns due to their persistence and toxicity in aquatic systems. This study investigates the efficacy of copper oxide-modified *Musa Parasidiaca* peel biochar-supported reduced graphene oxide (Cu/MPBC/rGO) as a novel adsorbent for removing IMI and ACE from aqueous solutions. The synthesized composite was characterized using scanning electron microscopy (SEM), Fourier Transform Infrared Spectroscopy (FTIR), X-ray diffraction spectroscopy (XRD) *etc*, to elucidate its morphology, surface chemistry, crystallinity, and porosity. Adsorption experiments were conducted to examine the influence of pH, contact time, adsorbent dose and adsorbate concentration. The adsorption kinetics followed the mixed order kinetic model, and the equilibrium data were best described by the Langmuir isotherm, indicating monolayer adsorption. Cu/MPBC/rGO exhibited high adsorption capacities of 62.19 mg g^{-1} for IMI and 32.78 mg g^{-1} for ACE. Reusability studies confirmed the material's stability and efficiency over multiple cycles. These findings proved the potential of Cu/MPBC/rGO as an efficient and sustainable adsorbent for the removal of neonicotinoid pesticides from contaminated water.

Received 2nd June 2025
Accepted 17th September 2025

DOI: 10.1039/d5ra03907j

rsc.li/rsc-advances

1. Introduction

Neonicotinoids, such as imidacloprid and acetamiprid, belong to a group of insecticides widely utilized in agriculture for their ability to manage pests effectively.[1,2] Nevertheless, their extensive application has raised concerns about environmental pollution, particularly in water and soil.[3] These substances persist in the environment and have been reported in various ecosystems, posing dangers to non-target organisms, including bees, other pollinators, aquatic creatures, and even humans.[4,5] Neonicotinoids have been classified by the United States Environmental Protection Agency (US EPA) as class II and III.[1,6] Given their high solubility, persistence and potential for harm, they have been listed on the european priority substances watch list and considered emerging contaminants.[7–9] Thus, it is essential to identify effective methods for eliminating neonicotinoids from polluted environments.

Conventional wastewater treatment plants are not equipped to remove these pollutants from water and soil, which has led to significant research attention. Various methods, including chemical oxidation,[10] coagulation and flocculation,[11] biodegradation,[12] ion exchange, ultrafiltration,[13] and adsorption[14] are utilized. Nonetheless, these approaches typically come with expensive operational costs, high chemical usage, significant sludge production, and low effectiveness.[15–17] The adsorption technique has been investigated and demonstrated to be the most effective method because it is easy to use, utilizes low-cost adsorbent materials, and is stable.[18–20]

Biochar, a carbon (C)-rich product acting as an adsorbent, has emerged as a promising material for environmental remediation, owing to its high surface area, porosity, and potential for surface modification to enhance adsorption capabilities.[21] Biochar derived from various waste biomasses, including *Musa paradisiaca* (plantain) peel,[18] *Carica papaya* seed,[20] coconut husk and shell,[22] rice straw,[23] bamboo and pine cones, offers

[a]*Department of Chemical Sciences, Redeemer's University, Ede, Osun State, P. M. B. 230, Nigeria. E-mail: bayodea@run.edu.ng; ajibolabay7@gmail.com*
[b]*Department of Industrial Chemistry, Faculty of Physical Sciences, University of Ilorin, Ilorin, P. M. B. 1515, Nigeria*
[c]*Department of Chemistry, Federal University Dutse, Jigawa State, Nigeria*
[d]*Department of Biotechnology and Chemistry, Vaal University of Technology, Private Bag X021, Vanderbijlpark 1900, South Africa*
[e]*Department of Chemistry, Kogi State University, Kabba, P. M. B. 222, Nigeria*
[f]*Department of Physical Sciences, Industrial Chemistry Programme, Landmark University, Omu Aran, P. M. B 1001, Nigeria*
[g]*School of Geography, Archaeology and Environmental Studies, Faculty of Science, University of the Witwatersrand, Johannesburg, South Africa*
[h]*Department of Chemistry, Faculty of Natural and Agricultural Sciences, University of Pretoria, Pretoria, South Africa*

a sustainable alternative for the removal of organic pollutants from contaminated systems. This approach not only helps remove harmful chemicals but also adds value to waste by repurposing it for environmental protection.

Recent advancements in biochar modification have focused on enhancing adsorption efficiency through the incorporation of nanomaterials, notably copper oxide (CuO) and reduced graphene oxide (rGO). Integrating CuO nanoparticles into biochar significantly enhances surface properties by functioning as active sorption sites and introducing Lewis acid centres, which facilitate strong interactions with nitrogen-containing functional groups found in compounds such as ACE and IMI.[18] Furthermore, CuO inherent antimicrobial characteristics suggest its potential as a dual-function material, effectively addressing both chemical and biological contaminants.[24,25] Research indicates that the utilization of CuO within carbonaceous matrices enhances pollutant uptake due to improved electron transfer and surface redox activity.[26]

On the other hand, rGO contributes by providing a large specific surface area and π-conjugated domains, which promote π–π stacking interactions with aromatic pollutants, including ACE and IMI.[27] Its residual oxygen functionalities further enhance adsorption kinetics and facilitate electron exchange processes.[28] Several studies have confirmed the efficacy of rGO-based composites in removing a diverse array of micropollutants such as pharmaceuticals and pesticides.

For example, Srikhaow *et al.* (2022) reported that conventional biochar from *Eucalyptus* woodchip achieved only 52.29 and 7.25% removal of neonicotinoids ACE and IMI.[29] Bi *et al.* (2025) reported that Co-NP3-1000, produced through carbonization of Zn/Co-ZIF at 1000 °C with a Zn/Co molar ratio of 3 : 1, exhibited exceptional adsorption capabilities for the efficient removal of neonicotinoids.[30] In West Africa, recent monitoring studies, such as those by Orikpete *et al.* (2025), have revealed alarming increases in neonicotinoid concentrations in the environment, attributed to agricultural runoff and pollination, underscoring the urgent need for locally adaptable and regenerative water treatment solutions.[31]

In a previous study by Bayode *et al.* (2023), the authors reported the effective removal of ibuprofen and diclofenac using Cu/Zn/PP/rGO for the adsorption process.[18] Building on this premise, this research investigates the synergistic effects of using a single metal source, CuO, and rGO modifications on biochar. The goal is to develop efficient, scalable, and sustainable solutions for the removal of neonicotinoids, specifically imidacloprid and acetamiprid, in environmental remediation.[32] Utilizing Musa paradisiaca (plantain peel) biomass for biochar production not only promotes waste valorization but also provides a cost-effective and environmentally friendly adsorbent material. Furthermore, the study will evaluate the performance of these modified biochars in both single and combined pollutant systems, addressing a critical gap in understanding the interaction of multiple pollutants during the adsorption process. Additionally, it will assess the effectiveness of using adsorbents in adsorption technology from both environmental and economic perspectives, employing cost Analysis.

2. Materials and methods

2.1. Materials

PTFE 0.22 μm membrane filters (Analitca), filter paper, cellulose nitrate filter (0.45 μ Sartorius stedim Germany), Nylon filter (47 mm, 0.45 μ, UNIFIL), magnetic beads, graphite (lab synth Brazil), methylene blue, hydrochloric acid, pottasium permanganate (lab synth Brazil), graphite (Lab synth Brazil), hydrogen peroxide (lab synth Brazil), millipore water, extran (lab synth Brazil), alcohol (99.8%, Neon Brazil), methanol (99%, HPLC grade, Sigma Aldrich, Germany), acetonitrile (99%, HPLC grade, Sigma Aldrich, Germany), sodium chloride (Sigma Aldrich, Germany), centrifuge, pipette, hydrazine, pipette tips.

2.2. Synthesis of the adsorbents

The *musa parasidiaca* peel was obtained from a roadside roasted plantain vendor at Akoda, Ede, Osun state (7° 43′ 5″ N, 4° 28′ 36″ E); they were washed with distilled water and sundried, and afterwards it was dried for 1 h in the oven at 105 °C. The obtained dried peel was pulverized in a grinder. The obtained powder is packaged and labelled MPBC.

2.2.1. Cu/MPBC ($CuCl_2$ + *musa parasidiaca* peel biochar). 4 g of copper chloride ($CuCl_2$) and 2 g of crushed *Musa paradisiaca* peel were combined in a beaker containing 10 mL of 0.1 M sodium hydroxide (NaOH). The mixture was continuously agitated for 20 minutes to ensure uniform interaction. Following this, the beaker was placed in an oven set at 105 °C for 24 hours to facilitate the impregnation process.

Subsequently, aliquots from the oven-dried composite were transferred to a furnace for calcination at 500 °C under an inert nitrogen (N_2) atmosphere. The temperature was increased at a rate of 5 °C per minute and maintained for 4 h. The resultant dark powder was then subjected to repeated washings using millipore water to remove residual NaOH and $CuCl_2$ from the surface of the copper-loaded *Musa paradisiaca* peel (Cu/MPBC). The pH of the wash filtrate was monitored and controlled until it stabilized at 7.0, at which point the washing process was ceased. The solid residue was then dried again in an oven at 105 °C and stored in an airtight container for future use.

2.2.2. Preparation of reduced graphene oxide (rGO). The graphene oxide was prepared by the Hummers' method, while the rGO was synthesized according to the protocol in our previous work.[18]

2.2.3. Cu/MPBC/rGO ($CuCl_2$ + *Musa paradisiaca* peel biochar + rGO). 2 g of Cu/MPBC was added to a 1 : 1 methanol–water solvent system containing 1 g of reduced graphene oxide (rGO). This mixture was agitated for 1 h using a magnetic stirrer to ensure homogeneity. Following this, the suspension was subjected to ultrasonic treatment for 3 hours to facilitate thorough mixing and minimize particle agglomeration. After sonication, the solution was decanted, and the resulting precipitate was dried in an oven at 105 °C for 7 h. The final powder product was stored in an airtight container to maintain its integrity.

2.2.4. Determination of point of zero charge (pHpzc). The salt addition method was adopted for pHpzc determination. The protocol was reported in our previous work.[33]

2.3. Characterization of Cu/MPBC/rGO

Infrared spectra were acquired utilising universal attenuated total reflectance (ATR) sampling on a PerkinElmer Spectrum 100 Fourier transform infrared (FTIR) spectrophotometer (USA). Surface morphology and elemental composition analyses were conducted with the LEO 440 scanning electron microscope, equipped with energy dispersive X-ray (EDX), operating at an accelerating voltage of 5 kV. X-ray diffraction measurements were performed using the PANalytical Empyrean powder X-ray diffractometer with Cu Kα radiation ($\lambda = 1.5419$ Å), operating at 40 kV and 40 mA.

2.4. Adsorption kinetic study

The preparation of the working solutions was conducted per the IMI and ACE standards, utilizing high-purity Millipore water to ensure the elimination of contaminants that could interfere with the results. To evaluate the method's linearity, a calibration curve was constructed, allowing for the determination of the coefficient of determination (R^2), which quantifies the reliability of the linear relationship between concentration and absorbance.

The calibration curve was established by preparing a series of standard solutions with concentrations of 1, 2, 5, 10, 15, and 20 mg L^{-1}, achieved through precise dilutions of a stock solution. Each solution was thoroughly mixed to ensure homogeneity before testing. The analysis was conducted using a UV-Vis spectrophotometer, which was calibrated and validated before use to ensure accuracy in measuring absorbance at the appropriate wavelengths corresponding to the analytes of interest. This meticulous approach facilitated the determination of concentration from measured absorbance values with a high degree of precision and reliability.

The batch adsorption kinetic study was conducted to evaluate the adsorption efficiency of the composite adsorbent Cu/MPBC/rGO for the pesticides ACE and IMI. This experiment utilized a 100 mL solution containing a concentration of 10 mg L^{-1} for each pesticide, while exactly 0.10 g of the adsorbent was introduced into the mixture. The experiment was carried out at a controlled temperature of 25 °C, conditions considered optimal for the adsorption process.

The mixture was thoroughly agitated for a total duration of 300 min to ensure adequate interaction between the adsorbent and the contaminants. To monitor the adsorption kinetics, 2 mL aliquots were carefully withdrawn at predetermined time intervals throughout the experiment. These samples were subsequently filtered through a 0.45 μm membrane filter to eliminate any particulate matter that might interfere with the analysis. The residual concentrations of ACE and IMI in the filtrate were quantified using a UV-Vis spectrophotometer, with specific detection wavelengths set at 246 nm for Acetamiprid and 270 nm for Imidacloprid. The analysis of the samples were carried out in triplicate.

The percentage removal efficiency of both pesticides was then calculated based on the initial and final concentrations using eqn (1), providing insights into the performance of the Cu/MPBC/rGO adsorbent in reducing pesticide levels in aqueous solutions.

$$R(\%) = \frac{C_0 - C_e}{C_0} \times 100 \quad (1)$$

C_0 is the initial concentration, and C_e is the final concentration of the contaminant.

2.4.1. Adsorption isotherm study. The adsorption isotherm study was conducted by systematically interacting 0.10 g of Cu/MPBC/rGO with varying concentrations of ACE and IMI insecticides, specifically ranging from 1 to 20 mg L^{-1}. The experimental setup is the same as that used in the adsorption kinetics phase to ensure consistency in data collection.

The suspensions were maintained under continuous stirring for 300 min to facilitate effective interaction between the adsorbent and the insecticides. Following this period, supernatants were carefully withdrawn using a syringe and filtered through a 0.45 μm membrane filter to remove any undissolved particles and ensure the clarity of the samples.

Subsequently, the remaining concentrations of ACE and IMI in the filtered samples were quantitatively analyzed using a UV-visible spectrophotometer, set to specific wavelengths of 245 nm and 270 nm to achieve optimal detection of the respective contaminant.

2.4.2. Effect of pH. The influence of pH on the adsorption process was optimized in this study. A specific amount of 0.10 g of Cu/MPBC/rGO composite was mixed with 100 mL of aqueous solutions containing 10 mg L^{-1} of both ACE and IMI. The pH of the solution was carefully adjusted within a controlled range from 2 to 12 by incrementally adding dilute sodium hydroxide (NaOH) or hydrochloric acid (HCl). Throughout the adsorption experiments, the pH remained stable, ensuring consistent conditions for the entire removal process. The mixture was continuously stirred at room temperature, maintained at 25 °C, to facilitate optimal interaction between the adsorbent material and the target contaminants in the solution.

2.4.3. The effect of Cu/MPBC/rGO dosage. The impact of varying doses of Cu/MPBC/rGO on the adsorption process was evaluated using 5 mg L^{-1} concentrations of 100 mL ACE and IMI solutions. The adsorbent quantities ranged from 0.005 to 0.10 g, with experiments conducted at pH 7 and under ambient conditions (20 °C) with continuous agitation.

2.4.4. Effect of anionic interference. The effect of anions on the adsorption of IBP and DCF was studied by adding 2.0 mM HCO_3, PO_4^{3-}, and SO_4^{2-} into 30 mg L^{-1} ACE and IMI solutions containing 0.20 g of the adsorbents. The mixtures were agitated for 480 and 120 min, respectively. At different time intervals, 2 mL aliquots were withdrawn from the samples. The concentration of the supernatant of ACE and IMI was determined using a UV-Vis spectrophotometer at 246 and 270 nm, respectively.

2.4.5. Effect of ionic strength. The effect of the initial ionic strength on the adsorption of ACE and IMP was studied by adding NaCl to 5 mg L^{-1} of ACE and IMI solutions containing 0.10 g of the adsorbent with concentrations of 0.05, 0.10, 0.15, and 0.20 mol L^{-1}. The mixtures were agitated for 240 min, respectively. At specific intervals, 2 mL aliquots were withdrawn from the samples. The concentration of the supernatant of ACE

and IMI was determined using a UV-Vis spectrophotometer at 246 and 270 nm, respectively.

2.4.6. Reuse efficiency. After the adsorption process, the ACE and IMI-laden Cu/MPBC/rGO were regenerated with ethanol and water using an ultrasonicator. After sonication, the solution was centrifuged at 10 000 rpm and dried for 6 h in the oven before it was used again.

3. Results and discussions

3.1. Characterizations

The functional groups found in MPBC, Cu/MPBC, and Cu/MPBC/rGO adsorbent were analysed using FTIR, as shown in Fig. 1A. For the MPBC adsorbent, the broad peak at 3500 cm^{-1} indicates the presence of hydroxyl (–OH) groups, which can be attributed to *Musa parasidiaca* peel biochar (MPBC). The peak near 1700 cm^{-1} suggests C=O stretching vibrations, likely originating from carboxylic or ketonic groups, while the band ranging from 1000 to 1500 cm^{-1} represents C–O stretching from alcohol, ester, or phenolic groups found in the plantain peel biochar.[18,34,35]

In the Cu/MPBC results, significant peaks were noted at 3250–3500 cm^{-1} for hydroxyl groups of polymeric compounds such as lignin or pectin that contain the functional groups of alcohols and phenols. Peaks at 1060 cm^{-1}, 1047 cm^{-1}, and 963 cm^{-1} correspond to C–O and C–H stretching. N–H bending vibrations of primary amines were recorded at 1609 cm^{-1}. Peaks between 500 and 963 cm^{-1} indicated the presence and formation of CuO on the adsorbent.[18]

The IR spectra of Cu/MPBC/rGO show a reduction in the peak around 3500 cm^{-1}, which may suggest the removal or transformation of hydroxyl groups during the reduction of graphene oxide. The absorption peak at 1620 cm^{-1} arises from the aromatic C–C bond, 1060 cm^{-1} from the alkoxy C–O group, 1170 cm^{-1} from the epoxy C–O stretching peak, 1400 cm^{-1} from the C–OH carboxyl group, 1740 cm^{-1} from the carboxyl C–O groups, 2900 cm^{-1} from C–H, and 3500 cm^{-1} from O–H groups.[18,25,36] rGO exhibits a significant decrease in the intensity of all oxygen-containing groups, indicating that graphene oxide is effectively converted to reduced graphene oxide.[25] The peak around 500 cm^{-1} confirmed the formation of CuO resulting from the modification with copper.[25]

The XRD confirmed the crystalline phase in the adsorbents Cu/MPBC and Cu/MPBC/rGO. Both adsorbent Cu/MPBC and Cu/MPBC/rGO showed the same peaks at 29.63, 36.44, 42.56, 61.42, and 73.54° as shown in Fig. 1B, which corresponds to (100), (111), (200), (220), and (311) planes. Indicating the cubic crystal structure of cuprous oxide Cu_2O (cuprite) with the space group Pn3m due to the reduction reaction of Cu(II) species to Cu(I) species (JCPDS 05-0667).

The monoclinic structure C_2/C cupric oxide (CuO) (Tenorite) was observed at 32.55, 35.74, 38.80, 48.81, 53.52, 58.20°

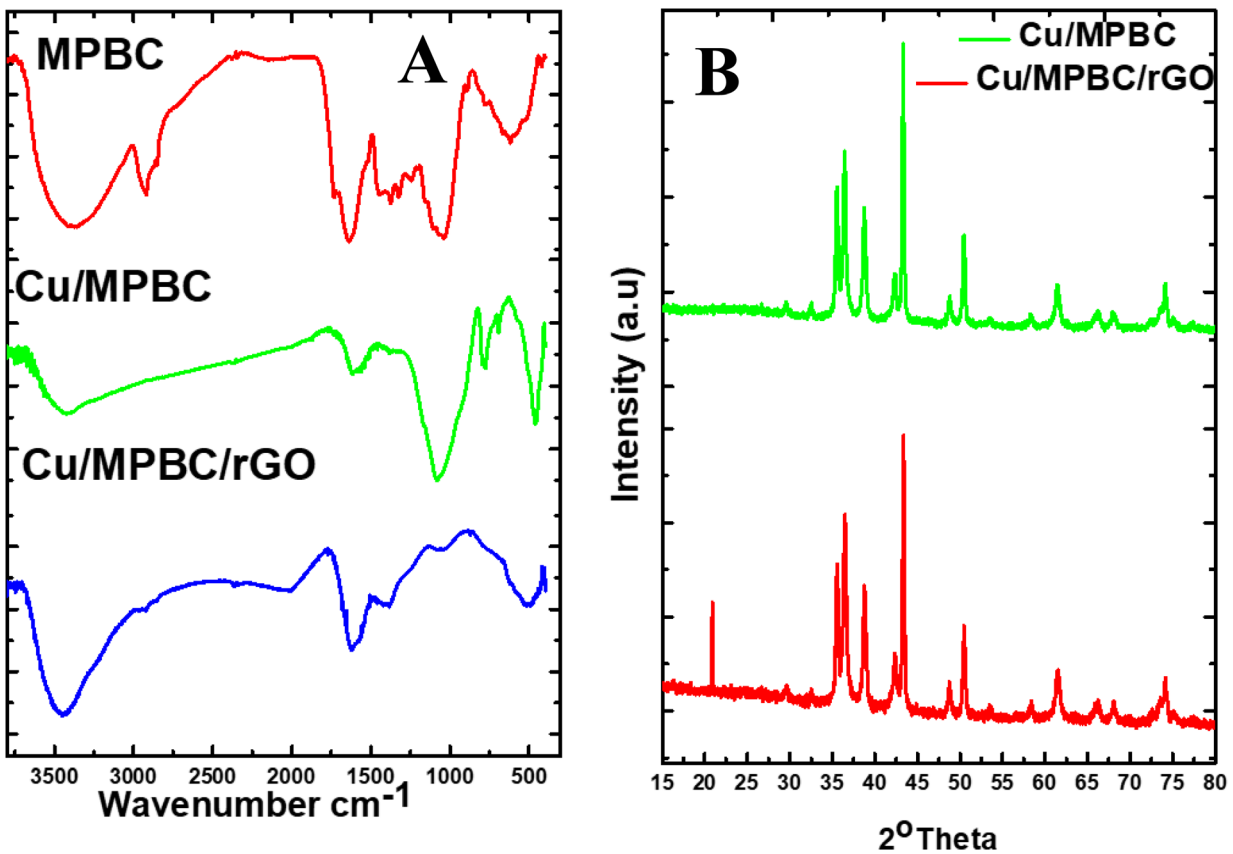

Fig. 1 (A). Fourier-transformed infrared spectroscopy spectra, (B) X-ray diffraction patterns of Cu/MPBC and Cu/MPBC/rGO.

corresponding to the (110), (002), (111), (202), (020), (113) plane. This is because of the addition of copper chloride and sodium hydroxide to the MPBC; the reaction (eqn (2)) leads to the formation of copper oxide (JCPDS 048-1548).

$$CuCl_2 + 2NaOH \rightarrow Cu(OH)_2 + 2NaCl \quad (2)$$

Upon calcination of the adsorbents, the copper hydroxide present produces copper oxide (tenorite) (eqn (3)):

$$Cu(OH)_2 \rightarrow CuO + H_2O \quad (3)$$

A sharp peak at 43° indicates the graphitized 101 plane, and the peak at 50° corresponding to the (100) indicates the turbostatic carbon resulting from the introduction of the biochar (MPBC). The sharp peak observed at 23.70° corresponds to the (002) plane, indicating the successful incorporation of the rGO into the adsorbent.

The Scherer equation, as stated below in eqn (4), was used to calculate the crystalline size of the adsorbents Cu/MPBC and Cu/MPBC/rGO.

$$D = \frac{K\lambda}{\beta \cos \theta} \quad (4)$$

where λ, β, θ, and D depict the wavelength, full width at half maximum, Bragg's angle for the given diffraction and the crystalline size.

The crystalline size was estimated to be 17.82 nm and 15.10 nm from the highest intense peak of the (200) plane.

The scanning electron microscope explored the surface morphology of the adsorbents Cu/MPBC and Cu/MPBC/rGO. The SEM micrograph of Cu/MPBC as seen in Fig. 2A, with the magnification highlighting structures around the micrometre scale, 2 μm bar, shows a rough, irregular surface with large, agglomerated particles. The visible structures traced in red oval demonstrated a porous, layered morphology in the carbonaceous skeleton, suggesting CuO particles are distributed over the MPBC matrix. The SEM micrograph of Cu/MPBC/rGO Fig. 2A, with a higher magnification scale bar of 200 nm, shows a finer, smoother sheet-like surface texture compared to Cu/MPBC/rGO. The texture appears to have finer granularity, possibly reflecting differences in CuO distribution or particle size, and the sheet-like texture observed is a result of the integration of the reduced graphene oxide in the adsorbent.

The EDX (Fig. 2C and D), which showed us the atomic composition tables, provides insight into the relative abundance of elements, with carbon and oxygen from the MPBC and rGO and copper representing the CuO modification. The increment in the carbon content in Cu/MPBC/rGO, as shown in Fig. 2D, is because of the rGO component.

3.2. Adsorption experiment

3.2.1. Optimising the various compositions of the adsorbents for the removal of ACE and IMI. The impact of each composition of the as-prepared adsorbent Cu/MPBC/rGO (CuO, MPBC and rGO) on the adsorption was evaluated using the

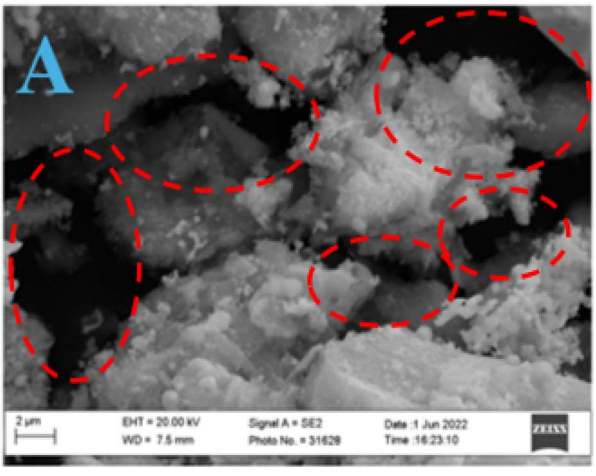

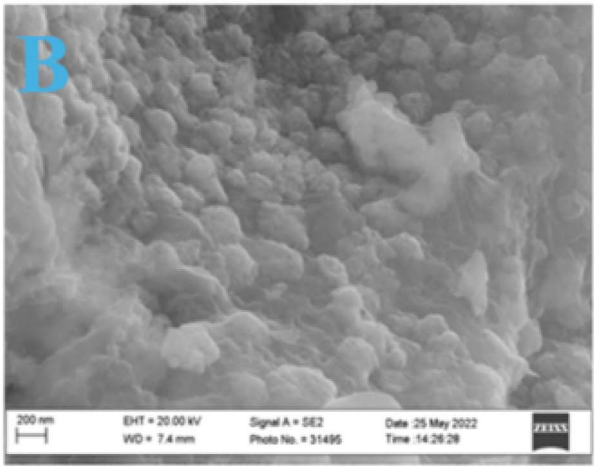

C

Element	Atomic Weight %
C	39.42
O	28.11
Cu	32.47
Total	100.00

D

Element	Atomic Weight %
C	42.98
O	25.48
Cu	31.62
Total	100.00

Fig. 2 Scanning electron microscopy images of (A) Cu/MPBC and (B) Cu/MPBC/rGO, energy-dispersive X-ray spectroscopy table of (C) Cu/MPBC and (D) Cu/MPBC/rGO.

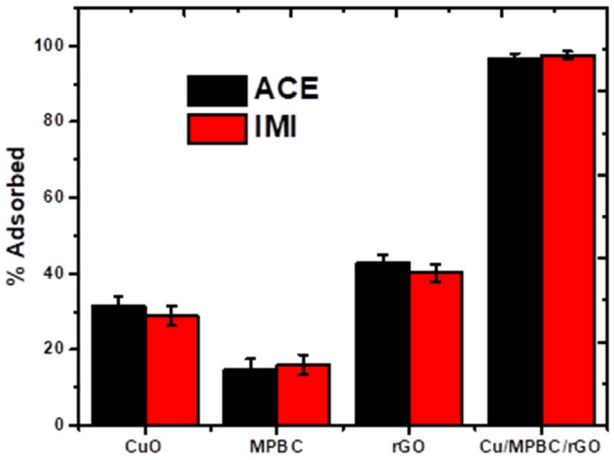

Fig. 3 Efficacy of the various components: copper oxide, MPBC, rGO, and the composite Cu/MPBC/rGO for the removal of IBP and DCF in water.

method described in Section 3.8. With samples taken at 300 min.

The result shown in Fig. 3 below indicates that CuO alone removed 31.43% and 28.91% of ACE and IMI, respectively. MPBC, which is the *musa parasidiaca* peel biochar, removed 14.66% and 15.99% for ACE and IMI, respectively. The rGO showed removal of 42.62% and 40.09% for ACE and IMI, respectively. When the three components were incorporated together of Cu/MPBC/rGO there was a tremendous improvement in the adsorption efficiency of the composite, showing 96.71% and 97.41% of ACE and IMI, respectively. This result proved the synergy effect of the three components, aiding in optimum adsorption efficiency.

3.3. Adsorption kinetics and isotherm

The adsorption kinetics experiment is used to investigate the effect of the contact time, ranging from 0 to 300 minutes, on the adsorption of ACE and IMI onto Cu/MPBC/rGO Fig. 4A and B.

In a bid to decipher the adsorption process for removing ACE and IMI from the adsorbent, three adsorption kinetic models, a three-parameter fractal-like pseudo-second-order kinetic model (FL-PSOM), a mixed-order kinetic model (MOE), and a two-parameter Elovich kinetic model were used for analysis.[37]

The kinetic parameter data for all the models utilized, along with their respective coefficient of determination (R^2) values, are presented in Table 1. To quantitatively evaluate the model's accuracy in representing the experimental data, the coefficient of determination (R^2) and equilibrium adsorption capacity (q_e) were employed.

Using the R^2 value, it was established that the experimental data for the adsorption of ACE and IMI are best described by the MOE kinetic model. This superior fit is attributed to the model's capability to incorporate both first and second-order kinetics, thus accurately characterizing complex adsorption processes. The optimal fit implies that the adsorption process for ACE and IMI involves multiple mechanisms or steps rather than a singular dominant pathway.[38,39]

The MOE model proposes that the adsorption of ACE and IMI is influenced by both physisorption and chemisorption, indicating a combination of diffusion-controlled and reaction-controlled processes.[39] The rate constant k_s reflects this

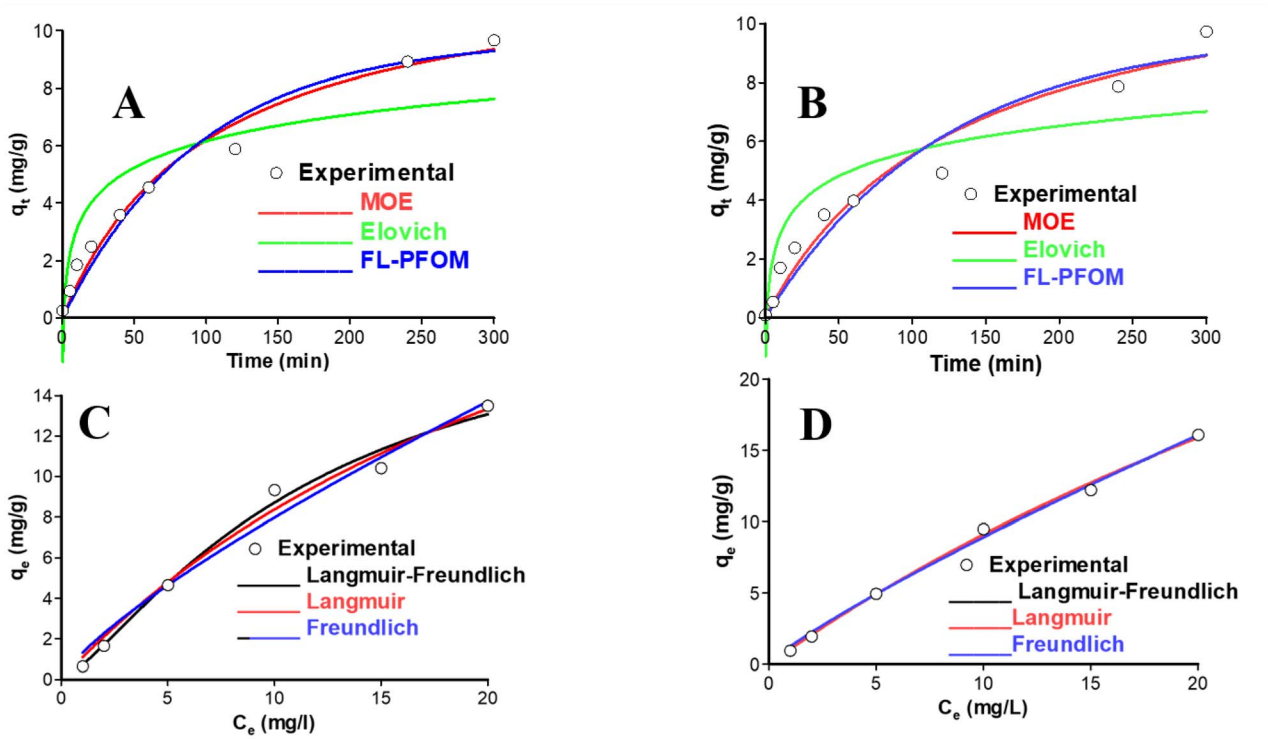

Fig. 4 Adsorption isotherm model fits of (A) ACE, (B) IMI adsorption by Cu/MPBC/rGO, (C) ACE, and (D) IMI adsorption by Cu/MPBC/rGO.

Table 1 Adsorption kinetics parameters of ACE and IMI on Cu/MPBC/rGO for three models

Kinetics	ACE	IMI
MOE		
q_e (mg g^{-1})	12.3142	12.5493
K_s (g mg^{-1} min^{-1}) Φ	0.0004	0.0039
Φ	0.9659	0.9616
R^2	0.9896	0.9778
FL-PFOM		
q_e (mg g^{-1})	9.7159	9.7338
K^2 (g mg^{-1} min^{-1}) θ	0.1017	0.0919
θ	0.1021	0.0909
R^2	0.9840	0.9714
Elovich		
K_c(mg g^{-1}) (min^{-1})	0.8181	0.8421
β (g mg^{-1})	2.9901	2.8433
R^2	0.9134	0.8939

combined kinetic behaviour, as evidenced by the small k_s values for both ACE (0.0004) and IMI (0.0039). These low values suggest a slower adsorption process potentially affected by weak interactions or mass transfer limitations, alongside mixed kinetic mechanisms. Furthermore, the higher q_e values in the MOE model (12.3142 mg g^{-1} for ACE and 12.5493 mg g^{-1} for IMI) indicate a strong interaction between the adsorbates and the adsorbents.

3.4. Isotherm kinetic study

Fig. 4C and D illustrates the adsorption isotherms used to estimate the quantity of ACE and IMI adsorbed onto the Cu/MPBC/rGO adsorbent at equilibrium. The experimental data were fitted into three equilibrium models: Langmuir, Freundlich, and Langmuir–Freundlich isotherm models. The experimental data indicates that the adsorption of both ACE and IMI onto the adsorbent Cu/MPBC/rGO follows this pattern: Langmuir > Freundlich > Langmuir–Freundlich isotherm models, based on the q_{max} and R^2 values presented in Table 2.

The Langmuir isotherm model showed the best fit with q_{max} values of 32.7759 mg g^{-1} for ACE and 62.1944 mg g^{-1} for IMI, indicating high adsorption capacities, especially for IMI. This suggests stronger molecular interactions or better compatibility with Cu/MPBC/rGO for IMI. The Langmuir model's fit indicates dominant monolayer adsorption, with slight heterogeneity for IMI, as supported by the Freundlich and Langmuir–Freundlich models.[18,37]

Table 2 Adsorption isotherm parameters of ACE and IMI on Cu/MPBC/rGO for three models

Isotherm	ACE	IMI
Freundlich		
K_f (mg g^{-1}) (L mg^{-1})$^{1/n}$	1.3248	1.2406
$1/n$	1.2822	1.1693
R^2	0.9886	0.9954
Langmuir		
Q_{max} (mg g^{-1})	32.7759	62.1944
K_L (L mg^{-1})	0.0343	0.0171
R^2	0.9928	0.9967
Langmuir–Freundlich		
q_e (mg g^{-1})	19.6260	19.9791
K_{LF}(L mg^{-1})	0.0844	0.0033
N	1.32107	0.8955
R^2	0.9823	0.9947

3.5. Effect of operational variables

3.5.1. pHpzc. The pHpzc is the pH at which the adsorbent surface has a net charge of zero. The adsorbent surface becomes positively charged if the solution's pH is less than the pHpzc, while it becomes negatively charged if the solution's pH is higher than the pHpzc.[40] The pHpzc of Cu/MPBC, the parent material, was observed to be 8.21. Upon modification with rGO, the pHpzc changed to 7.79, indicating an alteration in the surface chemistry of the adsorbent (Fig. 5). The adsorption process of positively charged imidacloprid and acetamiprid contaminants is favoured at a pH greater than the pHpzc. Therefore, the adsorption process by Cu/MPBC and Cu/MPBC/rGO should be optimal within the pH range of 2.0–7.0.

3.5.2. Effect of pH. The pH value is one of the most important factors controlling the adsorption of contaminants from water onto absorbents because it can affect the surface charge of the pollutant.[19] The adsorption of IMI and ACE was studied at different pH values of 2.0–12.0, with an initial concentration of 5 mg L^{-1} and an adsorbent dose of 0.1 g L^{-1}. The pK_a of both ACE and IMI are 0.70 and 11.12.[2,41] At pH 6, ACE and IMI exist mainly as weakly negatively charged species or neutral molecules due to the deprotonation of their nitro

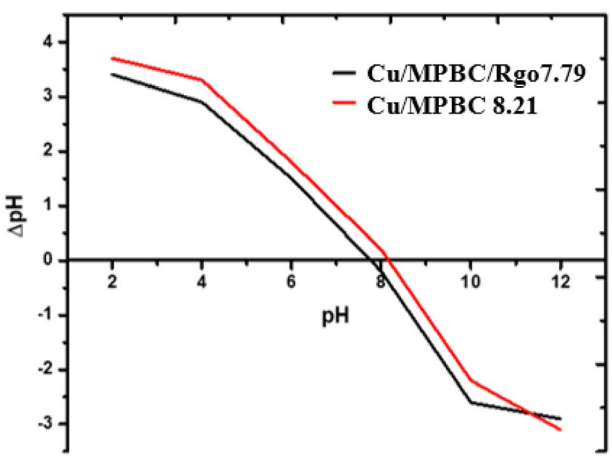

Fig. 5 pHpzc of Cu/MPBC and Cu/MPBC/rGO.

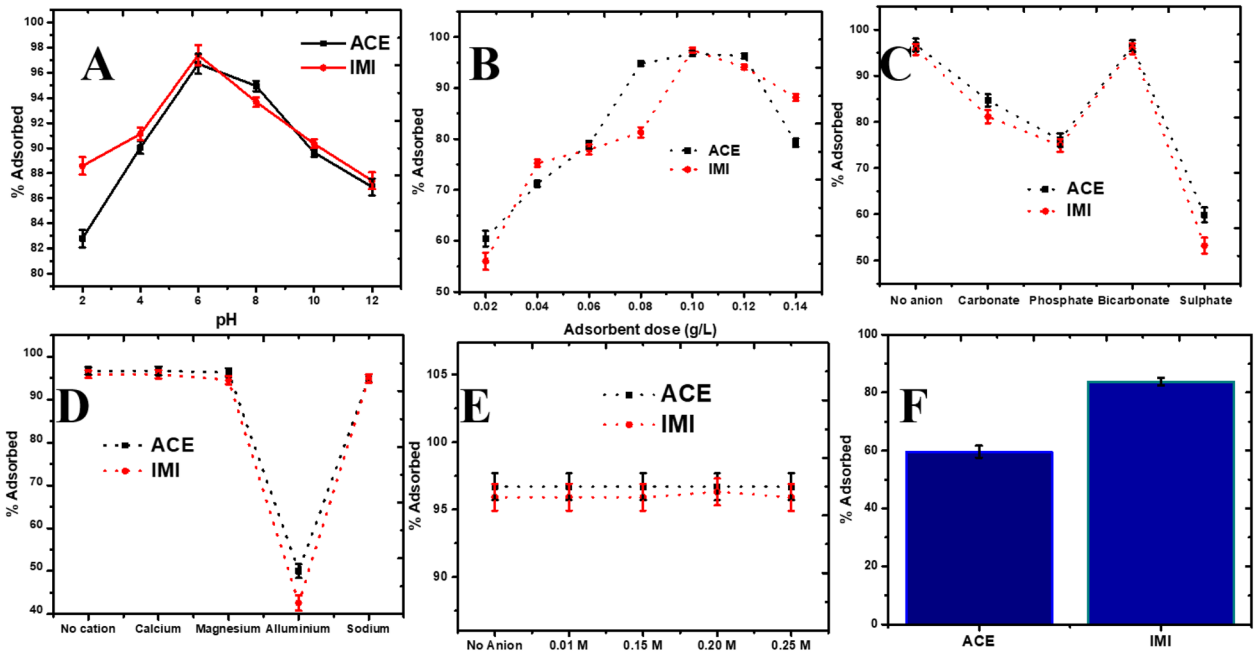

Fig. 6 Effect of (A) pH, (B) adsorbent dose, (C) anionic interference, (D) cationic interference, (E) ionic strength, (F) competitive adsorption on the adsorption of ACE and IMI onto Cu/MPBC/rGO. Error bars indicate the standard deviation of replicates ($n = 3$).

groups.[42] The result in Fig. 6A showed that the adsorption of both ACE and IMI was optimum at pH 6. At pH 6, the adsorbent's positive surface enhances interaction with the slightly negatively charged species, promoting weak electrostatic attraction. Also, at pH 6, ACE and IMI exhibit optimal hydrophobicity, reducing their solubility in water and enhancing their affinity for Cu/MPBC/rGO. Other reactions, such as van der Waals forces, hydrogen bonding, and Π–Π bonding, play a major role in adsorption because they depend on the pHpzc.

A decrease in adsorption efficiency was observed at pH 8. At pH > pHpzc, the adsorbent surface becomes negatively charged, thus repelling the negatively charged ACE and IMI species due to electrostatic repulsion. Also, the higher pH levels can increase the solubility of ACE and IMI, which leads to reducing the ACE and IMI affinity for Cu/MPBC/rGO.

3.5.3. Effect of Cu/MPBC/rGO dose. In a bid for sustainability and cost-effectiveness, the effect of adsorbent dose on the adsorption of 5 mg L^{-1} of ACE and IMI using different concentrations of Cu/MPBC/rGO (0.02 to 0.14 g L^{-1}) was studied (Fig. 6B). Removal efficiency increased with adsorbent dose from 0.02 to 0.10 g L^{-1}, achieving 96.70% and 97.40% removal rates for ACE and IMI, respectively, due to more active sites being available.[20] However, at 0.14 g L^{-1}, the removal efficiency dropped significantly, possibly due to agglomeration reducing surface area (Mao, Wang, Lin, Wang, & Ren, 2016). Thus, lower doses are more efficient and economical.[36,37]

3.5.4. Effect of anionic interferences. Various anions were examined for anionic interference, including phosphate, carbonate, sulphate, and bicarbonate. As shown in Fig. 6C, only bicarbonate did not affect the adsorption of ACE and IMI. This is likely due to bicarbonate's weak negative charge and low charge density compared to sulphate, carbonate, and phosphate, resulting in a low binding affinity for the Cu/MPBC/rGO surface. Bicarbonate's limited interaction prevents it from blocking or occupying active sites, and its equilibrium with carbonic ions reduces its availability for competition at active sites.

$$Cu–OH_2^+ + HCO_3^- \leftrightarrow Cu–HCO_3 + H_2O \quad (5)$$

Carbonate, phosphate, and sulphate ions are strongly negatively charged, competing with ACE and IMI for active sites. Carbonate and phosphate ions interact with the positively charged Cu/MPBC/rGO sites, forming stable complexes as shown in eqn (5)–(7), reducing the active sites available for ACE and IMI adsorption.

$$Cu–OH_2^+ + CO_3^{2-} \leftrightarrow Cu–CO_3^- + H_2O \quad (6)$$

$$Cu–OH_2^+ + PO_4^{3-} \leftrightarrow Cu–HPO_4 + H_2O \quad (7)$$

Similarly, the sulphate ion binds strongly to the positively charged site, leading to competition for the active sites with ACE and IMI (eqn (8)).

$$Cu–OH_2^+ + SO_4^{2-} \leftrightarrow Cu–SO_4 + H_2O \quad (8)$$

3.5.5. Effect of cationic interference. Different cations, such as calcium, sodium, aluminum, and magnesium were explored for the cationic interference study (Fig. 6D). It was observed that calcium and magnesium, divalent cations, and sodium, a monovalent cation, had negligible effects due to their weak interactions and lack of significant complexation or hydrolysis reactions. In contrast, aluminum, a trivalent cation

with high charge density, had a strong effect on the adsorption process. It reacts strongly with the negatively charged sites on the adsorbent or in the solution, forming stable complexes with functional groups such as hydroxyl and carboxyl present on the surface of the adsorbent (eqn (9)). Additionally, aluminum ions compete for active sites on the adsorbent surface, displacing ACE and IMI. Once the aluminium ion binds, it occupies the active sites, leading to fewer available sites for ACE and IMI.

$$Cu–OH_2^+ + Al^{3+} \leftrightarrow Cu–Al\ complex + H_2O \quad (9)$$

At near-neutral pH levels, aluminium ions undergo hydrolysis to produce aluminium hydroxide species (eqn (10)). These species precipitate and obstruct active sites, forming insoluble complexes with functionalities on the adsorbent, thereby diminishing their effectiveness.

$$Al_{3+} + 3H_2O \rightarrow Al(OH)_3 + 3H^+ \quad (10)$$

3.5.6. Effect of ionic strength. The effect of ionic strength on the adsorption of ACE and IMI onto Cu/MPBC/rGO was evaluated to simulate the presence of ions in environmental samples. The results indicated that increasing the NaCl concentration from 0.01 to 0.25 M did not reduce adsorption efficiency. This suggests that electrostatic interactions are not the primary mechanism driving the adsorption process; rather, non-electrostatic interactions such as π–π interactions, hydrogen bonding, hydrophobic interactions, and van der Waals forces predominate.[43,44]

3.5.7. Competitive adsorption of ACE and IMI. The adsorption competition between ACE and IMI was also investigated. It was observed that IMI exhibited higher adsorption compared to ACE (Fig. 6E). This may be attributed to IMI's delocalized electron system within its imidazolidine ring, enhancing its participation in π–π stacking interactions with the graphitic structure of rGO.[45] In contrast, ACE lacks such an extensive aromatic system, resulting in weaker π–π interactions.

Additionally, the nitroimine group in IMI provides a stronger bond acceptor than the cyano group in ACE, enabling IMI to form stronger hydrogen bonds with hydroxyl or carbonyl groups on the adsorbent. IMI is also slightly more hydrophobic than ACE due to its larger molecular size and less polar structure, making it more likely to adsorb onto the hydrophobic regions of the adsorbent surface (Table 3).

3.6. Cost analysis (TEA) for synthesis of 1 kg of Cu/MPBC/rGO

The cost analysis study was carried out to evaluate the cost and feasibility of the process of synthesis of the Cu/MPBC/rGO adsorbent. This helps to know if the process is cost-effective and sustainable on a large scale. The total cost of synthesis includes raw material sourcing, activation and calcination. Hence, the synthesis cost of Cu/MPBC/rGO, which proved to be effective for ACE and IMI removal in water, is estimated in Table 4 below.

In addition to its affordability, the Cu/MPBC/rGO material offers several notable advantages, including its sustainability due to the use of bio-based components, ease of separation from solution after application, and potential for regeneration and reusability in multiple adsorption cycles. These features make it not only a practical choice for various applications but also a proactive solution in the pursuit of environmentally friendly materials in the field of adsorption and remediation technologies. The synthesis cost of Cu/MPBC/rGO is approximately $267.09 per kilogram, which is significantly lower than that of commercially available adsorbents like single-walled Carbon nanotubes and multi-walled nanotubes, priced around $200 to $500 per gram. Beyond its cost-effectiveness, Cu/MPBC/rGO offers several advantageous features, including sustainability, straightforward separation processes, and both regeneration and reusability capabilities.

Table 3 Performance comparison of several adsorbents for the removal of ACE and IMI in water

Adsorbent	Contaminant	Adsorption capacity	% removal	References
Biochar from eucalyptus wood chip	ACE	4.87	—	29
	IMI	14.75		
Activated carbon	ACE	—	85.7	2
	IMI	—	85.0	
Sawdust of *Populus Nigra*	ACE	25.22	—	46
	IMI	25.65	—	
Modified pistachio shell-activated carbon	ACE	71.43	—	47
Moringa Olifera seed waste	ACE	70.22	—	48
AC/Fe_3O_4	ACE	192	—	49
Silver berry seed activated carbon	ACE	—	97	50
WHBC	IMI	7.41	—	51
Fe/Mg-WHBC		114		
TPAC	ACE	35.7	—	52
KBC	ACE	4014	—	53
Cu/MPBC/rGO	ACE	—	96.71	This study
Cu/MPBC/rGO	IMI	—	97.41	This study

Table 4 Cost analysis of Cu/MPBC/rGO

Processes	Subsection	Breakdown/Analysis	Cost (USD kg^{-1})	Quantity used/ price (USD)
Material processing	Plantain peel	20 g of kaolinite	0	30 g/0
	Graphite	25 g of graphite	71.22	25 g/67.20
Cu/MPBC/rGO synthesis	$CuCl_2$	Cost of the $CuCl_2$ used per kg	92.6	25 g/41.20
	NaOH	Cost of the NaOH used per kg	115.4	5.2 g/6
	H_2O_2	Cost of the H_2O_2 used per 2.5 L	51.6	1 L/25.8
	H_2SO_4	Cost of H_2SO_4 used per 2.5 L	144	50 mL/56.70
	H_3PO_4	Cost of H_3PO_4 used per 2.5 L	175	50 mL/45.50
	Hydrazine	Cost of hydrazine 100 mL		
	Drying cost	Power of oven *X* (kW) run time (h) *X* cost per hour KW h =	0.042	31 h/0.320
	Calcination cost	Power of furnace *X* (kW) run time (h) *X* cost per hour kW h =	0.042	4 h/0.040
	Sonication cost	Power of sonicator *X* (kW) run time (h) *X* cost per hour kW h =	0.042	5 h/0.050
Net cost of Cu/MPBC/rGO				242.81
VAT (10% of net)				24.281
Total cost				24.281

3.7. Reusability test

The reusability plot, as shown in Fig. 7, illustrates the performance of the Cu/MPBC/rGO nanocomposite over multiple adsorption–desorption cycles for the removal of imidacloprid (IMI) and acetamiprid (ACE). After each adsorption cycle, the used adsorbent was regenerated using ethanol and water *via* ultrasonication, then dried and reused under the same conditions.

The plot shows a slight but progressive decline in removal efficiency over five consecutive cycles. Initially, removal efficiency was above 96% for both IMI and ACE. By the fifth cycle, removal dropped to approximately 89% for ACE and 91% for IMI. This minimal decline demonstrates that Cu/MPBC/rGO maintains a high degree of structural integrity and functional activity even after repeated regeneration, confirming its robust stability and reusability.

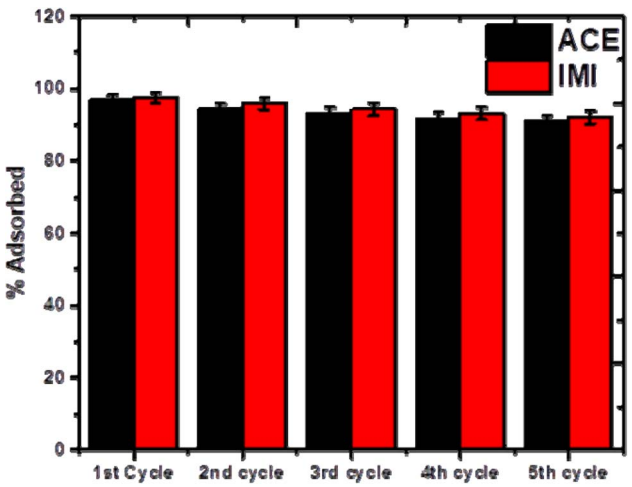

Fig. 7 Reuse efficiency of Cu@MPBC/rGO over five cycles to remove IMI and ACE in water. Error bars indicate the standard deviation of replicates ($n = 3$).

The decrease in efficiency is attributed to possible saturation of active sites, partial loss of surface functional groups during desorption, or incomplete removal of adsorbed contaminants during regeneration. Nonetheless, the composite exhibits excellent long-term usability, making it a cost-effective and sustainable candidate for real-world water treatment applications.

The sample underwent testing with ICP-OES, revealing that the Cu concentration was 0.06 mg L^{-1}, well within the permissible limits of 2 mg L^{-1} established by the World Health Organization (WHO). The minimal leaching observed could be attributed to high-temperature sintering or nanoparticle embedding, which may trap Cu particles deep within the matrix, exposing only a limited surface area for leaching.

3.8. Mechanism of removal of the ACE and IMI using Cu/MPBC/rGO

The high removal efficiency of ACE and IMI using the Cu/MPBC/rGO nanocomposite, as seen in Fig. 8, can be attributed to a blend of adsorption mechanisms, including physical, chemical, and electrostatic interactions. The synergistic combination of copper oxide nanoparticles (CuO), modified plantain peel biochar (MPBC), and reduced graphene oxide (rGO) enhances the multifunctional characteristics of the adsorbent, aiding in the strong and selective capture of pollutants.

A significant interaction that facilitates the adsorption of ACE and IMI is the π–π electron donor–acceptor interaction. Both neonicotinoids possess aromatic ring structures, with pyridine in acetamiprid and imidazolidine in imidacloprid, which can interact with the delocalized π-electron system present in rGO.[45] The graphitic domains on the surface of rGO allow π–π stacking with the electron-deficient aromatic rings of the pesticides, thereby improving molecular affinity and surface bonding.

At the optimal pH of 6, which is below the composite's point of zero charge (pzc = 7.79), the surface carries a slight positive

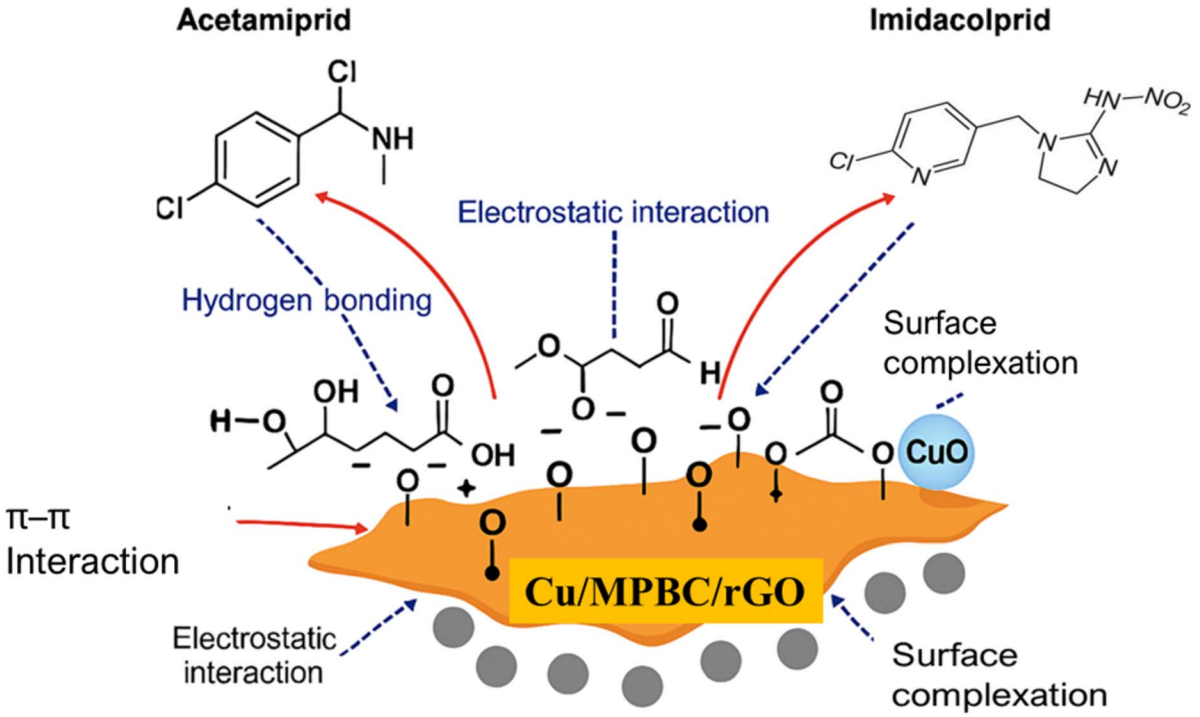

Fig. 8 The plausible adsorption mechanism of Cu/MPBC/rGO for the removal of ACE and IMI in water.

charge due to protonation of oxygen-containing functional groups (–COOH, –OH) on the biochar and rGO. Although ACE and IMI are predominantly neutral under these conditions, electronegative nitrogen atoms within their heterocyclic structures generate localized partial negative charges that can interact with the positively charged surface through dipole–charge attractions. This weak electrostatic component complements π–π interactions and other binding mechanisms, enhancing overall adsorption.[7]

In addition, hydrogen bonding plays a role in the adsorption process. The composite's surface, featuring functional groups such as hydroxyl and carboxyl groups from biochar and residual oxygen groups on rGO, can form hydrogen bonds with nitrogen atoms and electronegative centers found in the ACE and IMI molecules. These bonds help stabilize the adsorbed compounds on the surface, improving retention and selectivity. Another pathway for removal involves surface complexation with CuO nanoparticles.[54–56] The presence of CuO on the composite's surface offers Lewis acid sites that can coordinate with electron-donating nitrogen atoms in ACE and IMI. This coordination leads to chemisorption, creating stable surface complexes that enhance the selectivity and binding strength of the adsorbent. Therefore, the inclusion of CuO in the composite is vital for strengthening chemical interactions and increasing overall adsorption capacity.

Lastly, the porous nature of plantain peel biochar provides an abundance of micro- and mesopores that facilitate pore filling and physical adsorption. These pores serve as traps for the ACE and IMI molecules, allowing quick diffusion and entrapment. The elevated surface area provided by the rGO layers, coupled with the inherent porosity of the biochar matrix, significantly boosts the availability of active sites, further improving the composite's overall adsorption performance.

Overall, the removal of ACE and IMI by Cu/MPBC/rGO is influenced by a mixture of π–π stacking, hydrogen bonding, electrostatic interactions, surface complexation, and pore filling. The interaction of these mechanisms explains the high adsorption capacity, rapid kinetics, and excellent reusability observed in our work, positioning Cu/MPBC/rGO as a sustainable and multifunctional adsorbent for water systems contaminated with neonicotinoids.

4. Conclusion

This study presents the development and evaluation of a novel Cu/MPBC/rGO nanocomposite specifically engineered for the adsorption of the neonicotinoid pesticides imidacloprid and acetamiprid from aqueous media. The nanocomposite exhibits highly favourable surface properties and demonstrates exceptional thermal and structural stability, which significantly enhances its adsorption efficiency. Kinetic and isotherm analyses indicate that the adsorption mechanism is predominantly chemisorptive, following a monolayer adsorption model, with optimal efficiency observed at pH 6. The Cu/MPBC/rGO composite showcases impressive reusability, maintaining high removal efficiencies over multiple adsorption–desorption

cycles, which underscores its practical applicability in water treatment processes. It was established that the plausible mechanism of adsorption was through overall, the Cu/MPBC/rGO nanocomposite emerges as a promising, cost-effective, and environmentally benign solution for addressing neonicotinoid pesticide contamination in aquatic systems.

Author contributions

Conceptualization, B. A. A; methodology, B. A. A; formal analysis, B. A. A and S. S. E: resources, B. A. A: data curation, B. A. A and S. S. O.; writing – original draft preparation. B. A. A., writing – review and editing, B. A. A., O. O. T., H. B, A. A., O. P. I. and S. S. E, visualization, B. A. A and D. O. A; supervision, B. A. A.; project administration, B. A. A and D. O. A.; funding acquisition, B. A. A. All authors have read and agreed to the published version of the manuscript.

Conflicts of interest

The authors have no competing interests as defined by RSC or other interests that might be perceived to influence the results or discussion reported in this paper.

Data availability

The datasets used and/or analyzed during the current study are available from the corresponding author upon reasonable request.

Acknowledgements

Bayode Ajibola expresses gratitude to the African German Network for Excellence in Sciences (AGNES) for awarding the junior researcher grant, which facilitated a portion of this work. Bayode Ajibola Abiodun also acknowledges the Department of Chemical Sciences at the University of Padova, Italy, and Prof. Antonella Glisenti, leader of the Innovative Materials and Processes for Advanced Environmental Clean Technologies (IMPACT) group at the University of Padova, for providing a conducive working environment and assistance with characterizations.

References

1 A. Srikhaow, W. Chaengsawang, T. Kiatsiriroat, P. Kajitvichyanukul and S. M. J. M. Smith, *RSC Adv.*, 2022, **12**, 528.
2 J. Lu, Z. Zhang, X. Lin, Z. Chen, B. Li and Y. J. F. C. Zhang, *Food Control*, 2022, **131**, 108395.
3 X. Ji, Y. Liu, Z. Gao, H. Lin, X. Xu, Y. Zhang, K. Zhu, Y. Zhang, H. Sun and J. J. S. Duan, *Sep. Purif. Technol.*, 2024, **330**, 125235.
4 Y. Sun and X. Liu, *Appl. Surf. Sci.*, 2019, **485**, 423–431.
5 M. Qurie, M. Alkhatib, S. A. Bufo, L. Scrano, M. Khamis, I. Ayyad and R. J. D. Karaman, *Desalination Water Treat.*, 2021, 178–186.
6 M. O. Barbosa, N. F. F. Moreira, A. R. Ribeiro, M. F. R. Pereira and A. M. T. Silva, *Water Res.*, 2016, **94**, 257–279.
7 Y. Ma, Y. Qi, L. Yang, L. Wu, P. Li, F. Gao, X. Qi and Z. Zhang, *J. Clean. Prod.*, 2021, **292**, 126005.
8 N. E. Federoff, M. R. Barrett, R. P. Parker and V. Allen, *Problem formulation for the imidacloprid environmental fate and ecological risk assessment*, United States Environmental Protection Agency, 2008.
9 W. Hayat, Y. Zhang, I. Hussain, S. Huang and X. Du, *Ecotoxicol. Environ. Saf.*, 2020, **188**, 109891.
10 A. Derbalah, M. Sunday, R. Chidya, W. Jadoon and H. Sakugawa, *Health*, 2019, **17**, 254–265.
11 F. C. Gaioto, M. C. Matheus, B. M. de Souza-Chaves, J. C. Campos, T. A. Barra, D. de Almeida Azevedo and M. Dezotti, *Braz. J. Chem. Eng.*, 2024, **41**(4), 1109–1125.
12 X. Zhang, Y. Huang, W.-J. Chen, S. Wu, Q. Lei, Z. Zhou, W. Zhang, S. Mishra, P. Bhatt and S. Chen, *Environ. Res.*, 2023, **218**, 114953.
13 F. C. Gaioto, M. Matheus, B. M. de Souza Chaves, J. C. Campos, T. A. Barra, D. de Almeida Azevedo, J. P. Bassin and M. W. de Carvalho Dezotti, *Treatment and reuse of a pesticide-containing wastewater by a combination of physicochemical, biological and membrane processes*, 2023.
14 Y. Li, Y. Li, G. Bi, T. J. Ward and L. J. E. S. Li, *Sep. Purif. Technol.*, 2023, **30**, 47516–47526.
15 B. Yao and Y. Zhou, *Sep. Purif. Technol.*, 2024, 1–33.
16 Y. Zhang, W. Zhu, Y. Wang, X. Li, J. Lv, J. Luo and M. Yang, *Pharmacol. Res.*, 2024, **209**, 107415.
17 J. Wei, X. Wang, C. Tu, T. Long, Y. Bu, H. Wang, P. Jeyakumar, J. Jiang and S. Deng, *Environ. Int.*, 2023, **178**, 108044.
18 A. A. Bayode, M. T. Folorunso, B. Helmreich and M. O. Omorogie, *ACS Omega*, 2023, **8**, 7956–7967.
19 A. A. Bayode, H. Badamasi, J. A. Olusola, S. S. Durodola, O. K. Akeremale, O. T. Ore, B. Helmreich and M. O. Omorogie, *ACS Omega*, 2024, **47**, 375–386.
20 A. A. Bayode, F. O. Agunbiade, M. O. Omorogie, R. Moodley, O. Bodede and E. I. Unuabonah, *Environ. Sci. Pollut. Res.*, 2020, **27**, 9957–9969.
21 N.-A. O. Offiong, O. T. Ore, D. O. Aderibigbe, A. A. Bayode, O. S. Dabo and O. K. Akeremale, in *Biochar for Environmental Remediation*, Elsevier, 2025, pp. 169–189.
22 A. Ajien, J. Idris, N. Md Sofwan, R. Husen and H. J. W. M. Seli, *Environ. Res.*, 2023, **41**, 37–51.
23 W. Ahmed, S. Mehmood, M. Mahmood, S. Ali, A. Shakoor, A. Núñez-Delgado, R. M. A. Asghar, H. Zhao, W. Liu and W. Li, *Environ. Pollut.*, 2023, **326**, 121405.
24 P. Bhavyasree and T. Xavier, *Curr. Res. Green Sustainable Chem.*, 2022, **5**, 100249.
25 S. Jabeen, V. U. Siddiqui, S. Rastogi, S. Srivastava, S. Bala, N. Ahmad and T. Khan, *Mater. Today Chem.*, 2023, **33**, 101712.
26 M. Shaw, D. Samanta, S. Bera, M. K. Mahto, M. A. Salam Shaik, S. Konar, I. Mondal, D. Dhara and A. J. I. C. Pathak, *Inorg. Chem.*, 2022, **61**, 14568–14581.
27 A. A. Bayode, M. T. Folorunso, B. Helmreich and M. Omorogie, *ACS Omega*, 2023, **8**, 7956–7967.

28 N. Roy, K. Kannabiran and A. J. C. Mukherjee, *Chemosphere*, 2023, **333**, 138912.
29 A. Srikhaow, W. Chaengsawang, T. Kiatsiriroat, P. Kajitvichyanukul and S. M. Smith, *RSC Adv.*, 2022, **12**, 528.
30 L. Bi, L. Shi, K. Wang, J. Li, X. Tao, P. Liu, X. Li and J. Li, *Sep. Purif. Technol.*, 2025, **354**, 129292.
31 O. F. Orikpete, K. N. Kikanme, T. D. O. Falade, N. M. Dennis, D. R. Ejike Ewim and O. O. Fadare, *Chemosphere*, 2025, **372**, 144057.
32 W. Li, B. Liu, Z. Wang, K. Wang, Y. Lan and L. Zhou, *Environ. Sci. Pollut. Control Ser.*, 2020, **395**, 125094.
33 A. A. Bayode, E. M. Vieira, R. Moodley, S. Akpotu, A. S. de Camargo, D. Fatta-Kassinos and E. I. Unuabonah, *Chem. Eng. J.*, 2020, 127668.
34 A. O. Dada, A. A. Inyinbor, B. E. Tokula, A. A. Bayode, K. S. Obayomi, C. O. Ajanaku, F. A. Adekola, K. O. Ajanaku and U. J. E. R. Pal, *Environ. Res.*, 2024, **252**, 119046.
35 A. A. Bayode, F. O. Agunbiade, M. O. Omorogie, R. Moodley, O. Bodede and E. I. Unuabonah, *Environ. Sci. Pollut. Res.*, 2020, **27**, 9957–9969.
36 A. Parsaie, N. Rahbar and M. J. R. S. Baezat, *Int. J. Environ. Anal. Chem.*, 2021.
37 A. A. Bayode, S. S. Emmanuel, S. O. Sanni, F. Lakhdar, L. Fu, J. Shang and H.-J. Fan, *Chem. Eng. J.*, 2025, **302**, 120843.
38 M. O. Omorogie, M. T. Agbadaola, A. M. Olatunde, B. Helmreich and J. O. Babalola, *Green Chem. Lett. Rev.*, 2022, **15**, 51–60.
39 M. O. Omorogie, F. O. Ilesanmi, M. O. Alfred and B. Helmreich, *Chem. Eng. J.*, 2022, **46**, 20918–20931.
40 A. A. Bayode, E. M. Vieira, R. Moodley, S. Akpotu, A. S. de Camargo, D. Fatta-Kassinos and I. Unuabonah, *Chem. Eng. J.*, 2021, **420**, 127668.
41 R. Boumaraf, S. Khettaf, F. Benmahdi, R. Masmoudi, M. Belarbi and A. Ferhati, *Biomass Convers. Biorefin.*, 2024, 1–19.
42 J. R. Domínguez, T. González, S. Correia and E. M. Domínguez, *Environ. Res.*, 2021, **197**, 111021.
43 G. Wang, T. Sun, Z. Sun and X. Hu, *Appl. Surf. Sci*, 2020, **532**, 147411.
44 L. Bi, L. Shi, K. Wang, J. Li, X. Tao, P. Liu, X. Li and J. Li, *Separ. Purif. Technol.*, 2025, **354**, 129292.
45 X. Li, S. Fan, Y. Zhang, D. Li, C. Su, Z. Qi, H. Liang, S. Gao and M. Chen, *Bioresour. Technol.*, 2023, **386**, 129513.
46 A. Ullah, S. Ahmad, A. Gul, S. Khan, M. Zahoor, M. N. Umar and R. Ullah, *Z. Phys. Chem*, 2024, **238**, 1647–1661.
47 M. Dolatabadi, H. Naidu and S. Ahmadzadeh, *J. Clean. Prod.*, 2021, **316**, 128226.
48 M. M. Elkammah, *Assiut Univ. Bull. Env. Res.*, 2024, **27**(2), 74–85.
49 Y. L. Safe, V. Springer and M. Avena, *J. Environ. Chem. Eng.*, 2023, **11**, 111135.
50 R. Boumaraf, S. Khettaf, F. Benmahdi, R. Masmoudi, M. Belarbi and A. Ferhati, *Biomass Convers. Biorefin.*, 2024, 1–19.
51 X. Ji, Y. Liu, Z. Gao, H. Lin, X. Xu, Y. Zhang, K. Zhu, Y. Zhang, H. Sun and J. Duan, *Sep. Purif. Technol.*, 2024, **330**, 125235.
52 S. G. Mohammad, S. M. Ahmed, A. E.-G. E. Amr and A. H. Kamel, *Molecules*, 2020, **25**, 2339.
53 X.-W. Yao, X. Chen, M.-L. Chen, N.-J. Feng, L.-Y. Tong, Y.-Q. Yi, W. Qian and Z.-H. Diao, *Process Saf. Environ. Prot.*, 2024, **186**, 808–818.
54 P. S. Pauletto, S. F. Lütke, G. L. Dotto and N. P. G. Salau, *J. Mol. Liq.*, 2021, **336**, 116203.
55 A. Mandal, A. Kumar and N. Singh, *J. Environ. Manag.*, 2021, **295**, 113104.
56 A. Srikhaow, E. E. Win, T. Amornsakchai, T. Kiatsiriroat, P. Kajitvichyanukul and S. M. Smith, *RSC Adv.*, 2023, **8**, 26147–26157.